Numerical Simulation of Tropical Cyclone Mora Using a Regional Coupled Ocean-Atmospheric Model

NISHTHA AGRAWAL,[1] VIVEK KUMAR PANDEY,[1] and PRASHANT KUMAR[2]

Abstract—Tropical storms (TS) are highly sensitive to the behavior of nearby oceans, and the only way to improve their predictability is to include all the possible factors contributing to their genesis and motion. The present study evaluates the response of air–sea coupling on TS Mora, which occurred during the pre-monsoon season of 2017. Mora is simulated using a non-hydro-static regional atmospheric modeling system coupled to a regional ocean modeling system model. The observations show a low-level Rossby wave in the atmosphere during the storm genesis. There was also evidence of increased sea surface height simultaneously in the form of a downwelling Kelvin wave at the west coast of the Bay of Bengal. The present study emphasizes the relationship between near-surface oceanic and atmospheric circulation patterns. We have tried to elucidate the process with the help of dynamical equations and model solutions. We also analyze the pivotal role of the atmospheric Rossby wave in the formation of the coastal Kelvin wave. The Kelvin wave seems to produce a warm pool required to form a low-pressure system, which further gave rise to the tropical storm Mora. The changes in the temperature and salinity profile within the ocean subsurface layers during storm passage are further used for inferences regarding the vertical structure of the upper ocean due to wind-generated mixing. The model analysis reveals that the ocean and atmospheric counterparts responsible for storm genesis are well recorded in the coupled model when compared to the observations. It was found that air–sea coupling in the model made it possible to realistically capture ocean and atmospheric responses.

Keywords: Tropical cyclone, model coupling, ROMS, RAMS.

1. Introduction

Tropical cyclones (TCs) are one of the major natural hazards which affect the livelihood and economy of nearby coastal areas. The strong winds, storm surge and lightening produced around the path of these storms can have devastating effects on the local population and economy. Primary rainbands of TCs lie in a range of a few thousand kilometers, but their strongest and most disastrous impact is seen within a horizontal range of only a few kilometers from their center, and therefore they can also be beneficial for remote areas in need of precipitation for different uses. Moreover, the wind stress produced by these storms helps in vertical mixing of the underlying ocean, which can play an important role in redistribution of heat, energy cascade and marine ecosystem health. TCs are observed to form over warmer ocean bodies under suitable atmospheric stability and wind shear conditions. They obtain their energy from the surface fluxes of heat and moisture from the ocean. This energy perturbs the basic state of the atmosphere and creates the potential for convection and precipitation (Srinivas et al. 2016). On the other hand, cyclone-induced wind stress tends to result in turbulent mixing in the upper ocean layers, which cools the ocean surface via Ekman suction and acts as a negative feedback to the cyclone (Bender et al. 1993; Schade and Emannuel 1999; Bosart et al. 2000; Lin et al. 2005). Thus, the TC is direct linked to the thermodynamic properties of the ocean throughout its life span.

Numerous studies have reported on the response of the underlying ocean surface to the effects TCs. This includes the generation of cold and saline wake, changes in mixed and barrier layers, and upwelling of

[1] K. Banerjee Centre of Atmospheric and Ocean Studies, Institute of Interdisciplinary Studies, Nehru Science Centre, University of Allahabad, Allahabad 211002, India. E-mail: vivekbhuoa@gmail.com

[2] Department of Applied Sciences, National Institute of Technology Delhi, Narela 110040, India.

water due to divergence at the surface (Yan et al. 2017; Mawren and Reason 2017; Sun et al. 2018; Veeranjaneyulu and Deo 2019). Zhang et al. (2017) showed that energy spread due to the TC tends to distort the vertical stratification and dynamics of the underlying ocean. Qui et al. (2019) showed the existence of a barrier layer and its connection to sea surface temperature/sea surface salinity (SST/SSS) changes during the passage of TCs. Different studies have provided much useful information about the air–sea interaction of TCs after they achieve genesis, but information about the accurate state of their development and underlying circulation patterns has remained elusive. Studies have reported that a large proportion of cyclones are formed in the presence of tropical waves such as the Madden-Julian Oscillation (MJO), equatorial Rossby (ER) waves, mixed Rossby-gravity (MRG) waves and Kelvin waves (Carlson 1969; Frank and Clark 1980; Landsea 1993; Thorncroft and Hodges 2001; Hall et al. 2001; Bessafi and Wheeler 2006). It has been observed that the formation and propagation of these waves enhances the genesis potential of cyclones by strengthening the updrafts, increasing the low-level vorticity and altering the wind shear patterns (Frank and Roundy 2005). The propagation of tropical waves affects the ocean surface as well by imposing wind-generated forcing and radiative differences. These differences in turn form distinct patterns of upwelling/downwelling zones and give rise to important meteorological phenomena. For example, Rohith et al. (2019) have shown that MJO-induced wind stress transfers mechanical energy to the ocean which is responsible for intraseasonal fluctuations in sea-level and mass budget. Similarly, Sreenivas and Gnanaseelan (2014) showed that zonal wave changes in the central and eastern equatorial Indian Ocean are associated with the downwelling coastal Kelvin wave in the Bay of Bengal, which plays an essential role in cyclogenesis. In the present study, we have tried to elucidate this process via dynamical equations and model solutions. The objective of the proposed study was to analyze the effect of easterly waves on the downwelling coastal Kelvin wave and cyclogenesis associated with it. For this, we have used the non-hydrostatic Regional Atmospheric Modeling System (RAMS) coupled to the Regional Ocean Modeling

System (ROMS) via the Model Coupling Toolkit (MCT). The physical mechanism for the generation of the Kelvin wave is first described via dynamical equations, and we then analyze the formation of a warm pool and cyclogenesis associated with it. The effect of cyclogenesis on the upper ocean is further analyzed via model results. The remainder of the paper is organized as follows: Section 2.1 describes the basic features of the RAMS and ROMS models, the model coupling procedure, simulation details and sources of other data sets used. Section 2.2 provides a brief description of the storm background, Sect. 3 presents an analysis of the accuracy of the model outputs, and we conclude the work with Sect. 4.

1.1. Model Description and Data Used

Regional model coupling has seen tremendous growth in recent decades, and various state-of-the-art coupled models have been developed for comprehending different meteorological processes (Bender et al. 1993; Warner et al. 2010; Sein et al. 2015, 2020; Sitz et al. 2017; Sun et al. 2019; Reale et al. 2020). For the present study, we have followed the methodology adopted by the Coupled-Ocean–Atmosphere-Waves-Sediment Transport (COAWST) model (Warner et al. 2010) for coupling of ocean and atmospheric models. COAWST couples different models to study their interaction in a unified manner, and presently includes ROMS as the ocean model, which is coupled to one atmospheric model [Weather Research and Forecasting (WRF)] and two wave models (SWAN and WW3). Following the COAWST design, we have added RAMS to the list of atmospheric models in this system. The Model Coupling Toolkit (MCT) was used as the coupler, and the Message Passing Interface (MPI) standard was used to perform data transfer corresponding to different nodes. The Spherical Coordinate Remapping and Interpolation Package (SCRIP) was used to interpolate RAMS (ROMS) data onto a ROMS (RAMS) model grid. The code is designed in such a way that the domain of the atmospheric model has to be greater than or equal to the ocean model's domain. All the data transfer procedures were followed according to Warner et al. (2010). The atmospheric model provides surface heat and

moisture fluxes, 2 m air temperature, mean sea level pressure, surface wind stress, and precipitation and evaporation quantities to ROMS and receives SST from the ocean model.

The atmospheric model component RAMS is a terrain-following non-hydrostatic regional model (Cotton et al. 2003; Saleeby and Heever 2013) that can be used for fine grid simulations of different weather and climatic events. It is able to capture important convection and microphysical processes at cloud-resolving scale. The model contains the Land Ecosystem–Atmosphere Feedback model, version 3 (LEAF-3) (Walko et al. 2000), which works equally well for land and ocean, to provide an estimate for surface and boundary layer processes. The other sub-models account for aerosol (NH_4NO_3 and $NaCl$), salt and dust particles. The model uses two-moment bulk microphysics to predict the details of eight hydrometeor particles including cloud droplets, drizzle, rain, pristine ice, snow, graupel, hail and aggregates (Meyers et al. 1997; Saleeby and Cotton 2004; Saleeby and van den Heever 2013). We have used ROMS as the ocean component of our coupled system; it is a hydrostatic, three-dimensional, free-surface S-coordinate ocean model which is widely used to study the circulation, mixing and sedimentation of different oceanic processes at different spatiotemporal scales. The computational kernel of this multipurpose marine modeling system is inbuilt with a quasi-monotonic advection algorithm, advanced conservation properties and higher-order spatial approximations which are sufficient to accurately capture coastal, estuarine, mid-ocean and sea-ice features (Haidvogel et al. 2008). Its updated mode-splitting algorithms magnify the local density fields without sacrificing computational efficiency, which helps resolve barotropic processes under the slowly varying baroclinic motion (Shchepetkin and McWilliams 2005). It provides generalized time-stepping algorithms that treat wave motion with extra caution. It has multiple suites for turbulent mixing, boundary layer, ecosystem and sea-ice processes that are suitable for almost all kinds of applications. It is also equipped with advanced data assimilation methods which are useful for ocean prediction.

The coupled ROMS–RAMS system was configured for the Bay of Bengal region for simulating TS Mora during the period of 26 May–30 May 2017. RAMS was set up with 7.5 km horizontal grid spacing, and model equations were solved every 30 s. The model top was set to 26.1 km with 38 vertical layers. The vertical grid spacing was set to 100 m at the surface, with a vertical stretching ratio of 1.1, and maximum grid spacing of 1500 m. The storm convection was resolved using the modified Kuo scheme, boundary layer processes were solved using the Mellor–Yamada turbulent kinetic energy (TKE) scheme, and radiation was handled using the Harrington (1997) radiation scheme. Two-moment bulk microphysics was used to compute the mixing ratio and concentration of different hydrometeor classes including cloud droplets, drizzle, rain, pristine ice, snow, aggregates and graupel (Walko et al. 1995; Saleeby and Van Den Heever 2013). The Land Ecosystem-Atmosphere Feedback model (LEAF) was switched on to represent heat and moisture exchange between the atmosphere and surface (Walko et al. 2000). The initial SST forcing was given from the Hybrid Coordinate Ocean Model (HyCOM). The data exchange from the ocean to atmosphere and atmosphere to ocean took place every 5 min. Lateral boundary nudging was applied to the five boundary grid points every 15 min throughout the simulation period to ensure that the overall evolution of Mora was captured and the convective organization was freely moving into the domain interior. The model top was also nudged every 150 s to filter out the vertically propagating gravity waves.

The response of the ocean was captured using ROMS run at 6.5 km resolution. There were 32 vertical layers, with surface and bottom stretching ratios set to 7 and 0.1, respectively. The domain bathymetry was extracted from the ETOPO2 (Smith and Sandwell 1997) topography data set. Surface forcing required to initialize the model was provided from 6-hourly NCEP/NCAR reanalysis. The initial and lateral boundary conditions were interpolated from HyCOM data. The model physics includes Mellor–Yamada turbulent closure for boundary layer mixing, and the K-profile parameterization (KPP) scheme (Large and Gent 1999) was used for vertical mixing. Since the clouds remain absent during model initialization and are calculated in future time steps based on the humidity profiles and instability

conditions, we initialized both in the model 24 h before the storm genesis (i.e. at 26 May 1200 UTC) so that the cloud conditions might achieve a realistic stage within the next few hours. The volume-averaged turbulent kinetic energy (TKE) provided by ROMS gained stability within 6 h of model initialization (figure not shown), which is considered to be the spin-up period for the model. The model equations were solved every 120 s, and the output files were written every hour. The model solutions were integrated for the next 96 h, i.e. up to 30 May 1200 UTC. Apart from model data, we also used reanalysis and satellite measurements to validate our results. The observations to validate model-estimated precipitation were obtained from the Tropical Rainfall Measuring Mission (TRMM), NASA, USA (https://disc.gsfc.nasa.gov/datasets/TRMM_3B42_7/summary). The measured precipitation was available every 3 h at 25 km resolution. The measures of storm track and intensity were taken from the storm report provided by the Indian Meteorological Department (IMD). The satellite SSTs were obtained as the merged microwave SST (9 km × 9 km horizontal resolution) from the remote sensing systems. For the comparison of surface salinity, we used weekly satellite observations at 70 km resolution from the Soil Moisture Active Passive (SMAP) data archive (Meissner and Wentz 2018). We also used the Hybrid Coordinate Ocean Model (HyCOM) reanalysis (0.08° × 0.08°) products to generate initial and lateral boundary conditions for our ocean model. Since HyCOM was the only reanalysis data available during the time period of Mora, we used the same data to compare the vertical profile of temperature and salinity from the model for future time steps. The buoy data is also obtained from the Indian National Centre for Ocean Information Services (INCOIS) corresponding to two mooring buoys, BD08 and BD10, as mentioned (see Fig. 1).

1.2. Brief Description of Cyclone Mora

Mora was observed as a low-pressure system in the southeast and adjoining central Bay of Bengal (Fig. 2) on 25 May 2017, 0300 UTC, under the influence of upper air cyclonic circulation and low wind shear. The storm position was retained for the
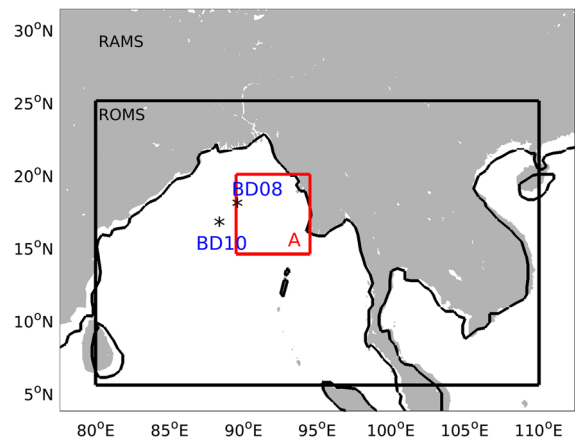

Figure 1
Experiment domains for RAMS and ROMS models. RAMS was run corresponding to the domain shown in the outer box, whereas the inner box (black) encompasses the ocean model domain. Box A shows the area over which the storm passed and is used to demonstrate the state of different area-averaged parameters
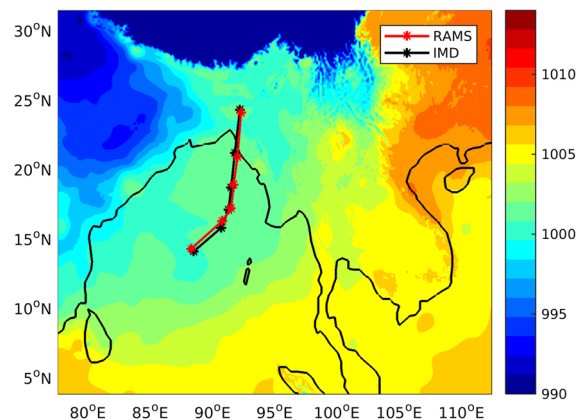

Figure 2
Distribution of sea level pressure (SLP) during the storm genesis. The black and red lines show the storm track given by the IMD and RAMS model, respectively

next few hours, after which it started intensifying and formed a well-marked low-pressure system during the early hours of 27 May. This low-pressure system transformed into a depression on 28 May 0000 UTC, and a deep depression within the next few hours (28 May 0900 UTC). It transformed into cyclonic storm MORA in the evening (28 May 1800 UTC). Thereafter, it kept on moving north-northeastward and transformed into a severe cyclonic storm on 29 May 1800 UTC, making landfall near Bangladesh on 30 May 0300 UTC. After making landfall, the system

weakened to a cyclonic storm, a deep depression and depression stages by the evening of the same day. Figure 2 shows the recorded track of Mora given by the IMD and the model solution. There exist different algorithms for tracking TCs by various studies (Neu et al. 2013; Lionello et al. 2016; Flaounas et al. 2016; Reale et al. 2019). In the present study, we have tried to locate the position of the lowest sea level pressure (SLP) manually using a code in order to obtain the modeled track of Mora.

The storm report provided by the Indian Meteorological Department (IMD) notes that the genesis of Mora occurred under the favorable environment of the Madden Julian Oscillation (MJO), which was observed to be in phase 2 during the storm intensification [Cyclonic Storm 'Mora' over Bay of Bengal (28–31 May 2017): A Report]. The active phase of the MJO near this region increased the atmospheric instability and upward motion which was sufficient for updrafts and higher convection. The observations indicate that the ambient flow was also under the active stage of low-level Rossby wave trains, as shown in Fig. 3. Low-level circulation can be fueled by the enhanced surface fluxes of heat and moisture. Therefore, Mora can be seen as coupled air–sea phenomena triggered by the Rossby waves in the troposphere and enhanced heat and moisture fluxes near the surface. The understanding of this process is the major objective of this study.

2. Results and Discussion

Figure 3 shows the satellite imagery of cloud disturbance on 26 May 1200 UTC. The image is obtained from the INSAT-3D soundings through MIR channel 3.9 μm available at the website of Meteorological and Oceanographic Satellite Data Archival Centre (MOSDAC), Space Application Centre (SAC), ISRO (https://www.mosdac.gov.in). The condition of tropical disturbance before the storm genesis is depicted in this picture. The observed cloud distribution is necessary to determine the distribution of cloud cover and relative humidity near the storm area. The cloud clusters can be clearly seen near the warm pool formed due to downwelling Kelvin waves. This shows that the atmospheric conditions were
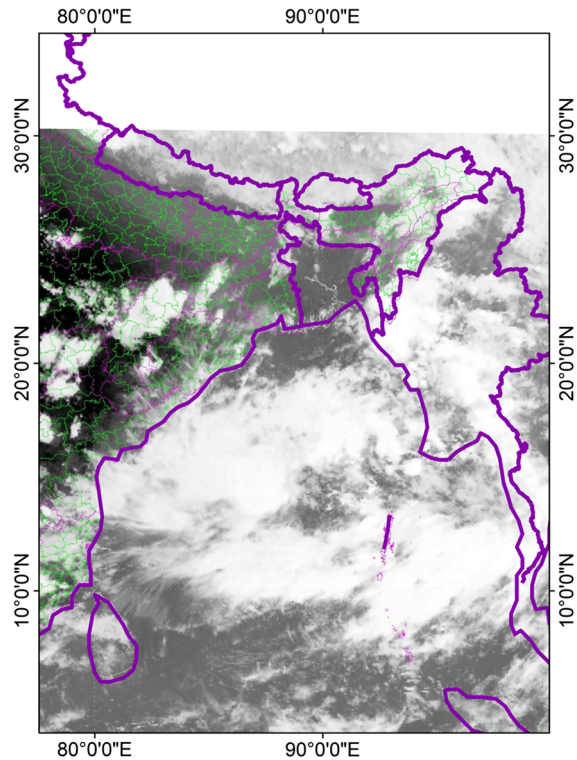

Figure 3
Satellite imagery showing the tropical disturbance during the storm genesis (26 May 1200 UTC). The circular cloud bands can be seen developing around the storm area near the western Bay of Bengal

favorable for storm genesis, and the downwelling Kelvin wave triggered cyclogenesis by forming the warm pool and increasing the instability. We have firstly investigated the impact of surface wind stress on initial sea surface height (SSH) distribution via dynamical equations and model results in Sect. 3.1 and 3.2. The SSH variations helped generate the warm pool which was crucial for the storm genesis. The response of the Bay of Bengal during the passage of the storm is shown in further subsections.

2.1. SSH Increment and Horizontal Divergence

Figure 4 represents the Hovmöller diagram corresponding to 850 hPa zonal winds averaged between the 15° S and 15° N latitude belt. It is taken from the North Carolina Institute for Climate Studies (NCICS) tropical monitoring website (https://ncics.org/portfolio/monitor/mjo/) which is created and maintained by Carl Schreck. The plot is generated by
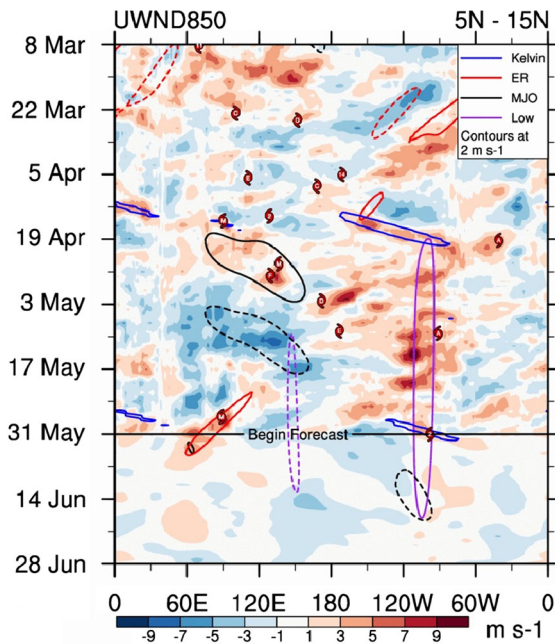
Figure 4
Hovmöller plot of zonal wind at 850 hPa; the horizontal axis shows the longitude range, whereas the vertical axis indicates the time range

Figure 5
Distribution of SSH during the model initialization period (26 May 1200 UTC). This is the genesis time for cyclone Mora

providing time, region, level and variable values. The presence of the Rossby wave can be easily detected in this figure within the 60° E–120° E longitude range during the storm period (25–31 May), thereby creating an easterly wind shear. It also indicates the presence of a tropical cyclone during that period. The significance of easterly waves for cyclogenesis is one of the most popular studies in the present decade, and its cyclogenesis is shown by various studies (Aiyyer and Thorncroft 2006; Kim et al. 2019). It is reported that westerly shear tends to deteriorate the storm, whereas easterly shear enhances it (Tuleya and Kurihara 1981). In general conditions, the strong winds at the low level tend to work on the ocean surface beneath them by displacing the warmer surface water and creating an upwelling zone. In the present study, the upwelling zone due to accumulation of water can be seen in the form of increased SSH (in meters) near the west coast of the Bay of Bengal (BoB) (see Fig. 5). The existing feature seems to be semipermanent and behaves according to the theoretical description of coastal Kelvin waves. Different studies have attempted to identify seasonal
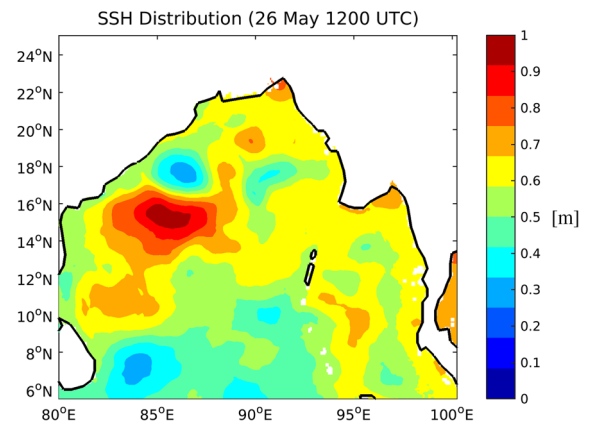
variability in the BoB (Rao et al. 2010; Nienhaus et al. 2012; Srinivas et al. 2014), almost all of which noted the presence of a coastal Kelvin wave during the pre-monsoon season near the western boundary of the BoB. Therefore, it is a downwelling coastal Kelvin wave which is trapped at the southwestern coast of India. The associated D20 anomalies propagated to the east up to a distance of a few kilometers and then continued to oscillate there (not shown here). The situation is evident in the initial condition being provided to the ROMS model. The SSH values are observed to be higher near the west coast throughout the storm period in the form of a coastal Kelvin wave. The wave helps form a warm pool in the ocean which becomes the desired zone of convergence. Therefore, Mora can be seen as the result of a westward-propagating Rossby wave enhancing low-level vorticity around the warm pool generated by the downwelling Kelvin wave in the western boundary of the BoB, which helped to increase the instability and formed a low-pressure system therein. Figure 6 shows the horizontal profile of SSH and the presence of a weak vortex around the maximum SSH value after 12 h of model initialization. Hence, Mora had its genesis over the warm pool generated by the coastal Kelvin wave which was a result of easterly wind shear. The coupling of this air–sea phenomenon can be well understood via detailed analysis of shallow-water equations as given below:
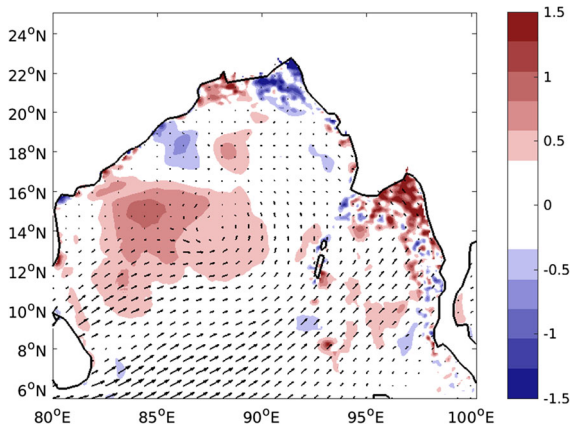
Figure 6
The distribution of SSH and wind stress vectors after 12 h of model initialization (27 May 0000 UTC)

$$g\frac{h'}{x} = fv' - \frac{u'}{t}, \qquad (1)$$

$$g\frac{\partial h'}{\partial y} = -fu' - \frac{\partial v'}{\partial t}, \qquad (2)$$

$$\frac{\partial h'}{\partial t} = -H\left(\frac{\partial u'}{\partial x} + \frac{\partial v'}{\partial y}\right), \qquad (3)$$

where f is the Coriolis parameter and (h', u', v') are the perturbations from the mean SSH, zonal and meridional velocities, respectively. Here we consider only the balance between pressure gradient, Coriolis force and horizontal acceleration. We do not impose the wind stress vector as source term initially in our equations.

On differentiating Eq. (1) w.r.t. x and Eq. (2) w.r.t. y, i.e,

$$g\frac{\partial^2 h'}{\partial x^2} = f\frac{\partial v'}{\partial x} - \frac{\partial^2 u'}{\partial x \partial t}, \qquad (4)$$

$$g\frac{\partial^2 h'}{\partial y^2} = -f\frac{\partial u'}{\partial y} - \frac{\partial^2 v'}{\partial y \partial t}. \qquad (5)$$

Differentiating Eq. (3) w.r.t. t and eliminating the terms involving u' and v' from (4) and (5), we get the following form:

$$\frac{\partial^2 h'}{\partial t^2} = -H\left[f\frac{\partial v'}{\partial x} - g\frac{\partial^2 h}{\partial x^2} - f\frac{\partial u'}{\partial y} - g\frac{\partial^2 h}{\partial y^2}\right]. \qquad (6)$$

After simplification, we get

$$\frac{\partial^2 h'}{\partial t^2} - c^2\nabla^2 h' = -fH\left[\frac{\partial v'}{\partial x} - \frac{\partial u'}{\partial y}\right], \qquad (7)$$

where $c^2 = gH$ is the speed of external gravity waves. The term on the right-hand side (RHS) of the above equation can be modified as

$$\frac{\partial^2 h'}{\partial t^2} - c^2\nabla^2 h' = -fH(\zeta + f) + f^2 H, \qquad (8)$$

the magnitude of f remains low in the tropics, and therefore we assume that its square can be negligible. Hence,

$$\frac{\partial^2 h'}{\partial t^2} - c^2\nabla^2 h' = -fH(\zeta + f). \qquad (9)$$

Considering the shallow-water vorticity equation,

$$\frac{1}{(f + \zeta)}\frac{D(f + \zeta)}{Dt} + \nabla \cdot U = 0. \qquad (10)$$

Thus a positive divergence decreases the absolute vorticity of a fluid parcel and vice versa.

2.2. Low-Level Wind Shear and Air–Sea Interaction

In the atmosphere, as the convergence zone strengthens, the intensity of the surface wind stress also increases. The wind stress influences the ocean by generating turbulent mixing in the upper layers, Ekman pumping deflects the fluid to create a divergence zone which consequently pushes the deeper cold and saline water to the surface. Therefore, the formulation of wind stress becomes of utmost importance for obtaining a reliable estimate of cooling near the surface in order to input the negative feedback to the atmospheric model again. The formulation of wind stress used in the present study is a function of the earth rotation velocities, surface density and friction velocity, which is obtained through Monin–Obukhov similarity theory used in the atmospheric model.

The model-calculated wind stress caused the surface water to pile up away from the center and create an upwelling zone near the center. Here, the storm-averaged minimum sea level pressure (MSLP) is represented to measure the extent of low-level convergence (LLC) around the storm area. Forcing due to LLC near the surface seems to induce the

divergence around the storm center, which accounts for the increased rate of upwelling near this region. Figure 7 shows the variation in the MSLP averaged over the storm area (89.5 E–94.5 E; 14.5 N–20 N) and resulting changes in Ekman pumping velocity, which is used as a measure of storm-induced upwelling near the storm area. The represented MSLP values were obtained from RAMS, and its response was measured according to the zonal and meridional components of surface wind stress given to ROMS. The extent of the Ekman pumping vector was obtained using the following expression:

$$U_E = X/\rho f, \tag{11a}$$

$$V_E = \Upsilon/\rho f, \tag{11b}$$

where X and Y are the wind stress vectors corresponding to zonal and meridional directions, respectively, and ρ is the density of ocean water. To obtain a better picture of this effect, we averaged these quantities around the coastal region whose horizontal range lies between 89.5° E–94.5° E longitude and 14.5° N–20.0° N latitude. We chose this box to see the effect of low pressure on Ekman suction. We see that as the pressure decreases, the storm intensity increases, and so the wind stress vector increases as well. This intensifies the upwelling near the storm area as the storm approaches this region under the radius of maximum winds. After the storm passes, the wind intensity tends to weaken, which also reduces the wind stress at the enclosed area, and therefore the intensity of upwelling is also
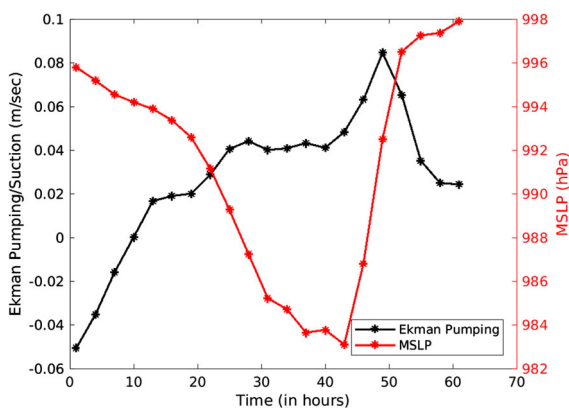

Figure 7
Variation in area-averaged MSLP and the Ekman pumping velocity as a measure of storm-induced upwelling

decreased at this stage. Thus, the storm-averaged Ekman pumping velocity shows that the occurrence of enhanced forcing near the surface causes upwelling, which is reduced after the storm passage.

Replacing the absolute vorticity from the RHS of Eq. (9) using (10) we get

$$\frac{\partial^2 h'}{\partial t^2} - c^2 \nabla^2 h' = F(\nabla \cdot U). \tag{12}$$

This equation establishes the relationship between horizontal divergence of ocean currents and disturbance in SSH.

Ekman established the relationship between horizontal divergence in ocean currents and wind stress curl using the following expression:

$$(\nabla \cdot U) = \frac{1}{\rho f}\left[\frac{\partial \tau^y}{\partial x} - \frac{\partial \tau^x}{\partial y}\right], \tag{13}$$

where $X = (\tau^x, \tau^y)$ is the horizontal wind stress vector.

From Eqs. (10) and (11), we have

$$\frac{\partial^2 h'}{\partial t^2} - c^2 \nabla^2 h' = Q\big((\nabla x X) \cdot \hat{k}\big). \tag{14}$$

This is an inhomogeneous wave equation in SSH whose source term Q is a function of wind stress curl. Its particular integral can be obtained by using Green's function in the following way

$$h'(x, y, t) = \iiint G(x, x', y, y' t, t') \\ Q(x', y', t')\mathrm{d}x' \, \mathrm{d}y' \, \mathrm{d}t'. \tag{15}$$

We can also have the same dependence of SSH on wind stress curl directly from Eq. (3)

$$\frac{\partial h'}{\partial t} = \frac{-H}{\rho f}\left[\frac{\partial \tau^y}{\partial x} - \frac{\partial \tau^x}{\partial y}\right], \tag{16}$$

for the given initial condition, $h'(x,y,0) = 0$. We have the following solution to this equation:

$$h'(x, y, t) = \int \frac{-H}{\rho f}\big((\nabla x X) \cdot \hat{k}\big)\mathrm{d}t. \tag{17}$$

This shows that the SSH of a given area decreases according to the integral of wind stress curl applied to that area.

The wind stress vector is directly linked with atmospheric circulation, as an increase in low-level relative vorticity results in high wind stress curl on

the ocean surface, which in turn results in greater divergence of ocean currents. Therefore, any atmospheric phenomenon affecting the low-level convergence has significant implications for SSH anomalies. For equatorial Rossby waves, we can simply remove the meridional component of the stress vector, which eventually results in

$$\frac{\partial h'}{\partial t} = \frac{H}{\rho f} \left[\frac{\partial \tau^x}{\partial y} \right]. \tag{18}$$

Therefore, the westward wind stress will tend to decrease the SSH of the area where it is implemented. The displaced water will be accumulated westward; if there is a western boundary on the other side, this accumulated wave will move southward (Gill 1982). This satisfies our understanding of the downwelling Kelvin wave during the presence of a low-level atmospheric Rossby wave. Therefore, the downwelling Kelvin wave is one such example that emerged due to the presence of low-level atmospheric Rossby waves.

2.3. Generation of Cold and Saline Wake

The extent of wind-induced mixing is often reflected in the difference in temperature distribution on the ocean surface. Figure 8 shows the difference in SST before and after the storm period using model

results and satellite observations in the left and right panels, respectively. The satellite-recorded SST cooling is around 3.5 °C near the northern coast of the BoB. The model-evaluated difference has a similar minimum magnitude around the storm area, and its spatial pattern shows relatively greater cooling in other areas surrounded by the storm as well. One possible reason might be the temperature distribution in reanalysis data, as shown in the middle panel of Fig. 8, which was used to provide initial and lateral boundary conditions for the ocean model. The ROMS-calculated SST is closer to the reanalysis even when we did not use any nudging in the ocean model. Figure 10 shows a comparison of SST obtained from the model and mooring buoys BD08 and BD10. The scatter plot reveals a strong linear relationship between model data and both buoys, with significant ($p < 0.01$) positive correlation coefficients of 0.94 (BD10) and 0.91 (BD08). Thus the intensity of temperature cooling near the storm area is accurately captured in the model throughout the simulation period.

The situation is similar with the SSS difference. Figure 9 shows the difference in pre- and post-storm surface salinity using the model (left) and satellite (right) data. The intensity of the model-produced SSS difference is stronger than that of the satellite difference. We can also see several negative values
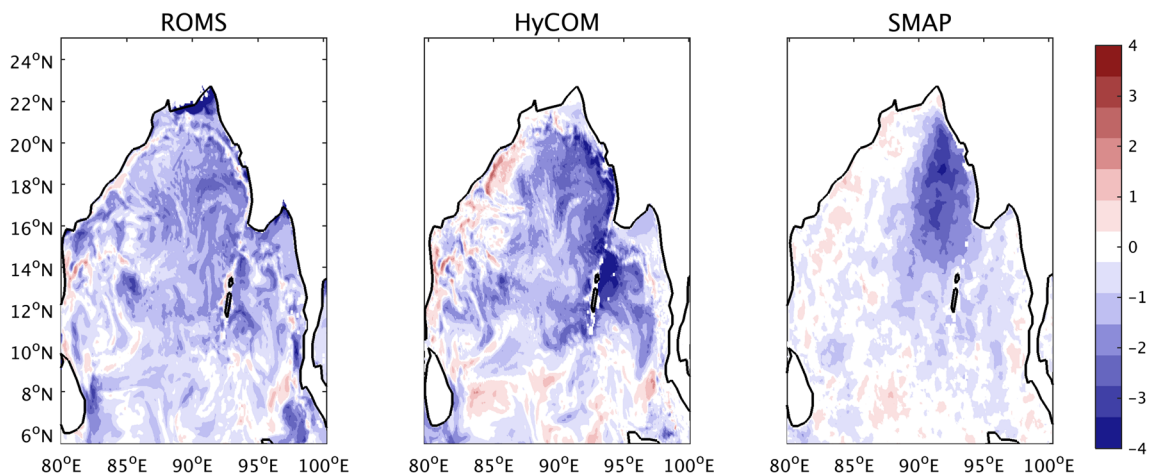

Figure 8
SST difference observed by the model (left), reanalysis (middle) and the satellite data (right). The difference is taken for the values of pre- and post-storm period
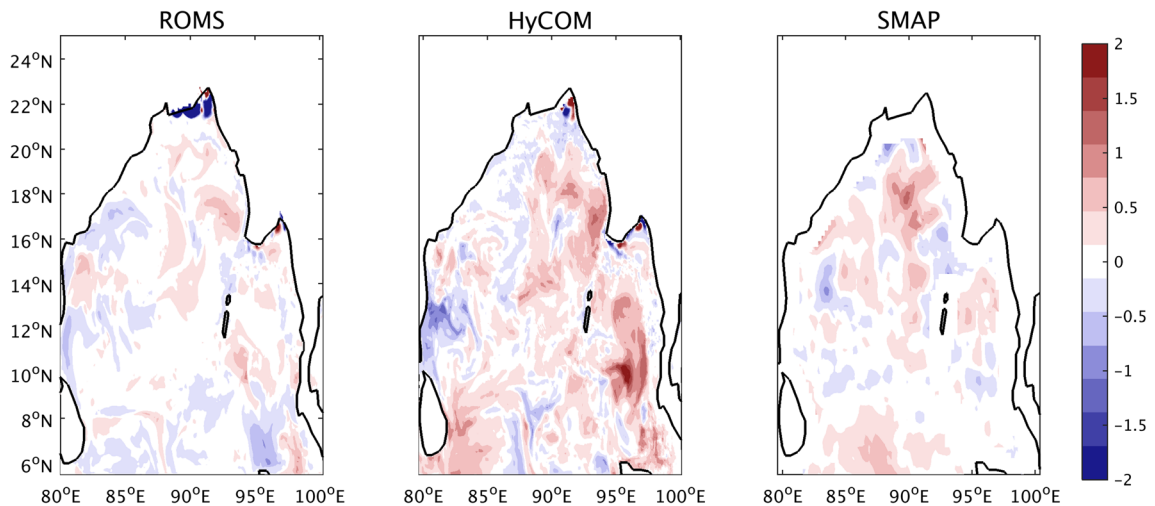
Figure 9

SSS difference observed by the model (left), reanalysis (middle) and the satellite data (right). The difference is taken for the values of pre- and post-storm periods

in the difference plot of the model data, which are absent in the difference plot of the satellite observation. The horizontal grid spacing of satellite data ($\sim$ 70 km) is much coarser than our model resolution ($\sim$ 6.5 km); therefore, we expect negligent effects in capturing small-scale disturbances in the satellite data. The maximum increase in salinity is around 1 PSU, which is still similar between the data sets (Fig. 10).

2.4. Vertical Profile of Temperature and Salinity

The storm has a significant effect on the subsurface properties of the ocean. The passage of the storm is related to strong mixing of up to several hundred meters of ocean that affects its physical, thermodynamic and chemical properties and the marine ecosystem to a large extent. Cloud canopy and high-intensity winds tend to cool the ocean surface by inhibiting incoming radiation from the sun and producing turbulence that causes mixing in the ocean. The wind stress-induced mixing deepens the mixed layer depth and changes the temperature profile. In Fig. 11, the upper panel shows the storm-averaged vertical temperature profile. The left panel shows vertical temperature profiles before and after the storm passage from ROMS, and the right panel shows

the same obtained from the HyCOM reanalysis. The temperature difference simulated by ROMS is close to the reanalysis data, although there remains a difference of 20–25 m in mixed-layer depth.

Wind-induced mixing and upwelling not only brings cooler water upward; it also brings saline and denser deep water to the surface. The lower panel of Fig. 11 shows the vertical salinity profile before and after the storm period. The distribution is shown with respect to ROMS and HyCOM data. It can be seen that ROMS has captured the denser and saline wake realistically when compared to the reanalysis. The model also reports the 20–30 m of upward shift in the halocline, which is reasonable based on the storm intensity and is also evident in the HyCOM results.

2.5. Precipitation

The basic RAMS fields were nudged slightly towards the reanalysis, so the validation of track and intensity becomes trivial, as they will automatically be closer to the observations. However, there is still uncertainty about the cloud conditions and precipitation rates, which are crucial for the radiation budget and ocean heat content. For our study, we compare the model-produced precipitation to the TRMM precipitation data set ($\sim$ 25 km) after 15 h, 30 h
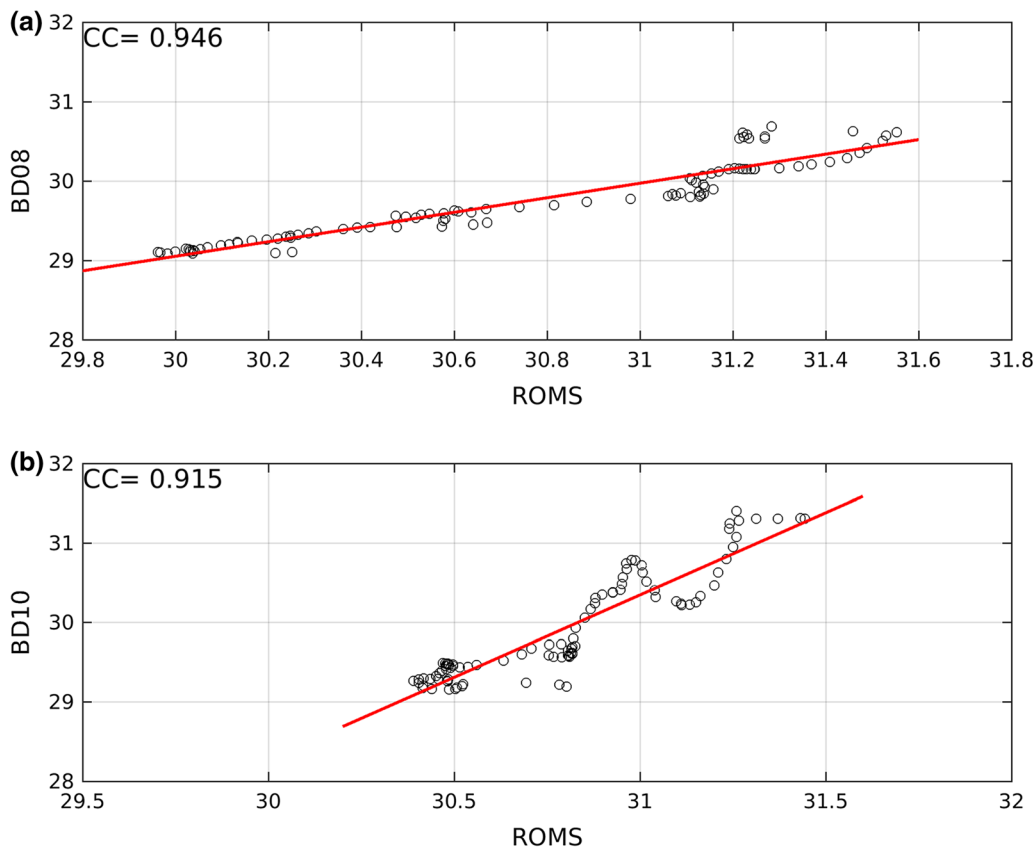
Figure 10
Scatter plot of ROMS and buoy SST for mooring buoys; **a** BD08; **b** BD10

and 54 h of storm intensification in Fig. 12. In this figure, the left and middle panels show the precipitation rate (in mm/h) provided by the RAMS and TRMM data sets. The model bias is shown in the right panel. Figure 12 shows that the model precipitation is simulated realistically throughout the simulation period, and the area of intense convection is also coincident when compared with the TRMM data set. The model is shown to have a wet bias near the inner core of tropical cyclone Mora, and the bias is drier in the outer core regions during the entire intensification period. Therefore, the position of rainbands seems to be shifted slightly rightward in the model when compared to the TRMM precipitation. This could be due to the position of the cyclone in the model, which appears to shift slightly rightward as compared to the observation. The difference in the track can arise for several reasons, including

systematic model error, induced background flow and model physics. These factors incorporate different subgrid scale processes, including land surface, planetary boundary layer and cloud microphysics. The different schemes are expected to give different results by making changes in diabatic heating, wind shear and updraft speed. The model behavior is consistent with the observations.

3. Conclusion

The present study intends to assess the capability of a coupled ROMS–RAMS system to simulate a TC event and its driving mechanism. It was seen that the cyclone was originated under the presence of a low-level atmospheric Rossby and external Kelvin wave. The downward Kelvin wave-induced warm pool
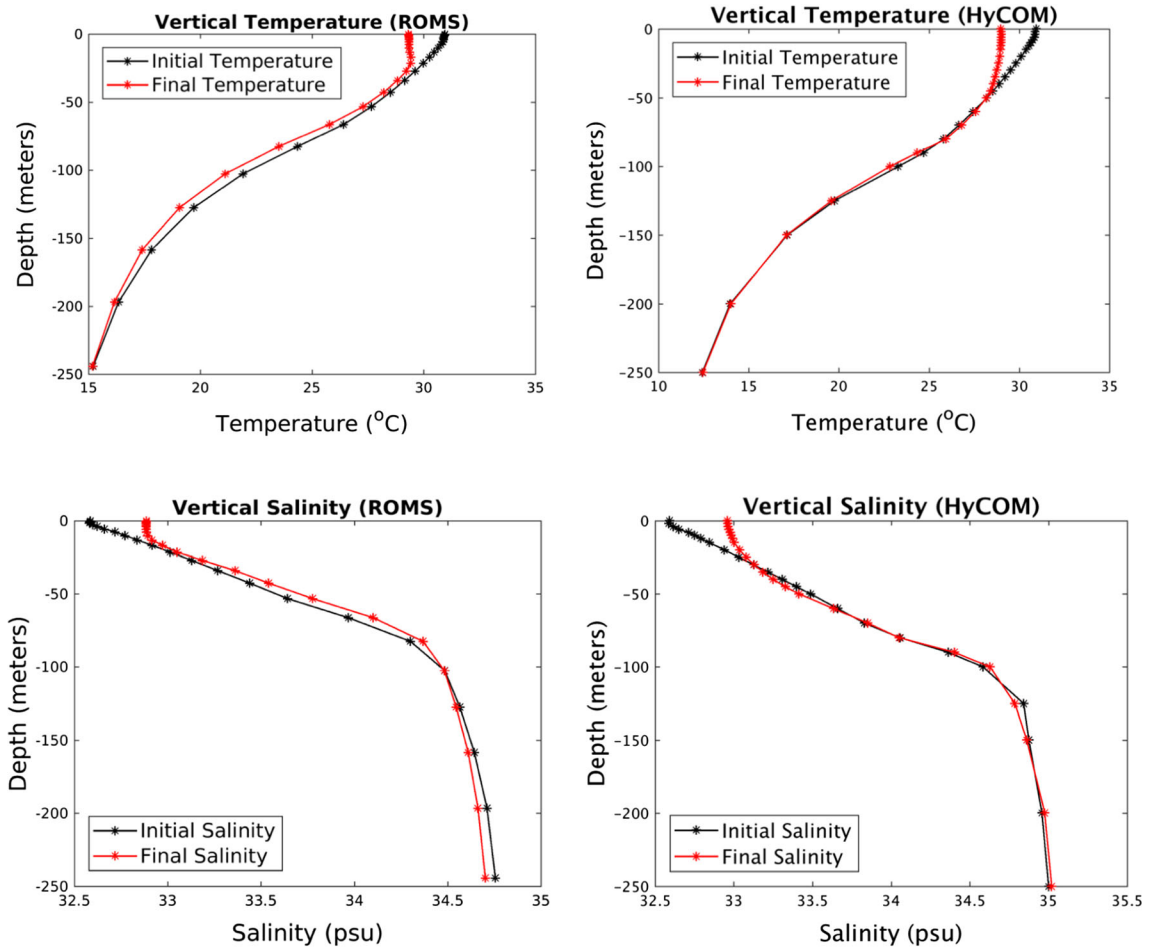
Figure 11
Vertical profile of temperature (upper panel) and salinity (lower panel) given by ROMS (left) and HyCOM (right) before and after passage of the storm. The values are averaged around the storm area as shown in the red box in Fig. 1

generated a favorable condition for LLC and cyclogenesis. The intensification of wind-induced upwelling is also consistent theoretically with the variation of SLP. We have not intended to show the storm track and intensity as the weak nudging towards the reanalysis was used in our atmospheric model; therefore, it was presumed that the cyclone track and intensity would be closer to the observations. It is shown that the storm-induced mixing and its feedback contribute significantly in evaluating the rate of precipitation. The analysis of the coupled model indicates that the storm-induced mixing is also captured realistically in our result, and that the SST cooling and SSS increment are reliable when compared to the satellite observations. The storm area-averaged cooling and salinity differences are closer to that depicted by the HyCOM data. The model-evaluated mixed layer depth and pycnocline are shifted slightly upward as the storm proceeds. Storm precipitation shows a wet bias when compared to the satellite data; however, the areas of intense convection are still coincident with the observations. Thus, each model seems to respond accurately to the forcing generated by the other, and both can be used for further applications.
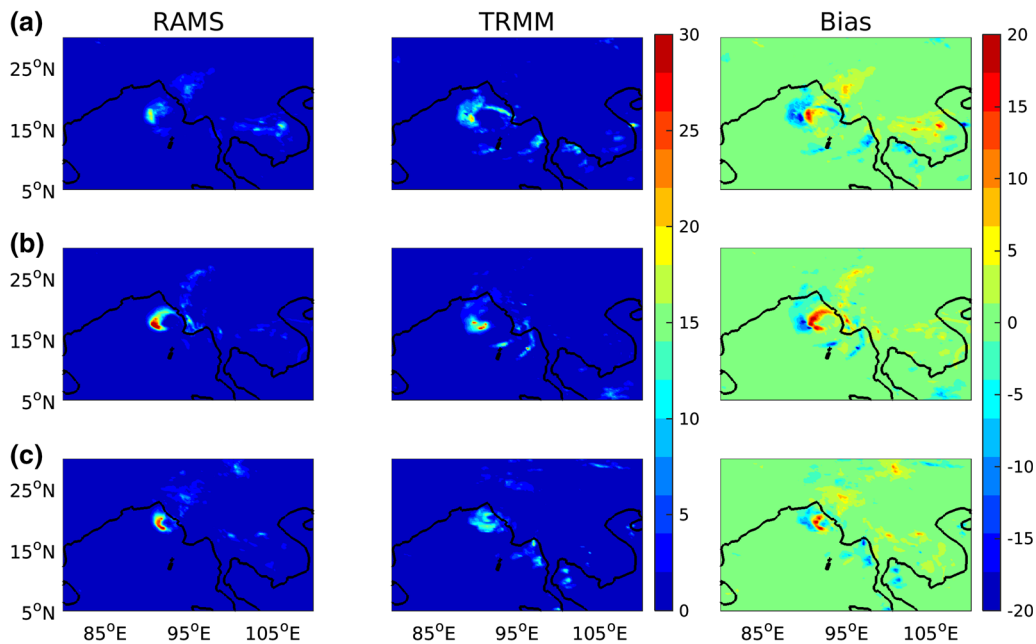
Figure 12

Precipitation rate (mm/h) captured by the model (left) and the TRMM (middle) data sets. The bias (model–TRMM) precipitation rate is shown in the rightmost panels. The values correspond to **a** 15 h, **b** 30 h and **c** 45 h periods of storm intensification

REFERENCES

Aiyyer, A. R., & Thorncroft, C. (2006). Climatology of vertical wind shear over the tropical Atlantic. *Journal of Climate, 19*(12), 2969–2983.

Aldrian, E., Sein, D., Jacob, D., Gates, L. D., & Podzun, R. (2005). Modelling Indonesian rainfall with a coupled regional model. *Climate Dynamics, 25*(1), 1–17.

Bender, M. A., & Ginis, I. (2000). Real-case simulations of hurricane–ocean interaction using a high-resolution coupled model: Effects on hurricane intensity. *Monthly Weather Review, 128*(4), 917–946.

Bender, M. A., Ginis, I., & Kurihara, Y. (1993). Numerical simulations of tropical cyclone–ocean interaction with a high-resolution coupled model. *Journal of Geophysical Research Atmospheres, 98*(D12), 23245–23263.

Bessafi, M., & Wheeler, M. (2006). Modulation of south Indian Ocean tropical cyclones by the Madden–Julian Oscillation and convectively coupled equatorial waves. *Monthly Weather Review, 134*, 638–656.

Bosart, L., Velden, C. S., Bracken, W. E., Molinari, J., & Black, P. G. (2000). Environmental influences on the rapid intensification

of Hurricane Opal (1995) over the Gulf of Mexico. *Monthly Weather Review*, *128*, 322–352.

Carlson, T. N. (1969). Synoptic histories of three African disturbances that developed into Atlantic hurricanes. *Monthly Weather Review*, *97*, 256–276.

Cotton, W. R., Pielke, R. A., Sr., Walko, R. L., Liston, G. E., Tremback, C. J., Jiang, H., et al. (2003). RAMS 2001: Current status and future directions. *Meteorology and Atmospheric Physics, 82*(1–4), 5–29.

Flaounas et al. (2016). Assessment of an ensemble of ocean-atmosphere coupled and uncoupled regional climate models to reproduce the climatology of Mediterranean cyclones. Climate Dynamics. https://doi.org/10.1007/s00382-016-3398-7.

Frank, N. L., & Clark, G. B. (1980). Atlantic tropical systems of 1979. *Monthly Weather Review*, *108*, 966–972.

Frank, W. M., & Roundy, P. E. (2005). The role of tropical waves in tropical cyclogenesis. *Monthly Weather Review*, *134*, 2397–2417.

Gill, A. E. (1982). *Atmosphere–Ocean Dynamics* (p. 662). New York: Academic Press.

Gustafsson, N., Nyberg, L., & Omstedt, A. (1998). Coupling of a high-resolution atmospheric model and an ocean model for the Baltic Sea. *Monthly Weather Review, 126*(11), 2822–2846.

Haidvogel, D. B., Arango, H., Budgell, W. P., Cornuelle, B. D., Curchitser, E., Di Lorenzo, E., et al. (2008). Ocean forecasting in terrain-following coordinates: Formulation and skill assessment of the regional ocean modeling system. *Journal of Computational Physics, 227*(7), 3595–3624.

Hall, J. D., Matthews, A. J., & Karoly, D. J. (2001). The modulation of tropical cyclone activity in the Australian region by the Madden–Julian Oscillation. *Monthly Weather Review*, *129*, 2970–2982.

Harrington, J. Y. (1997). *The effects of radiative and microphysical processes on simulated warm and transition season Arctic stratus* (Doctoral dissertation, Colorado State University).

Kim, D., Ho, C. H., Park, D. S. R., & Kim, J. (2019). Influence of vertical wind shear on wind-and rainfall areas of tropical cyclones making landfall over South Korea. *PLoS One, 14*(1), e0209885.

Krishna Kumar, K., Hoerling, M., & Rajagopalan, B. (2005). Advancing dynamical prediction of Indian monsoon rainfall. *Geophysical Research Letters, 32*, 8. https://doi.org/10.1029/2004GL021979.

Landsea, C. W. (1993). A climatology of intense (or major) Atlantic hurricanes. *Monthly Weather Review*, *121*, 1703–1713.

Large, W. G., & Gent, P. R. (1999). Validation of vertical mixing in an equatorial ocean model using large eddy simulations and observations. *Journal of Physical Oceanography, 29*(3), 449–464.

Lin, I. I., Wu, C. C., Emanuel, K. A., Lee, I. H., Wu, C. R., & Pun, I. F. (2005). The interaction of supertyphoon Maemi (2003) with a warm ocean eddy. *Monthly Weather Review*, *133*, 2635–2649.

Lionello, P., et al. (2016). Objective climatology of cyclones in the mediterranean region: A consensus view among methods with different system identification and tracking criteria. Tellus. ISSN 1600-0870

Mawren, D., & Reason, C. J. C. (2017). Variability of upper-ocean characteristics and tropical cyclones in the South West Indian Ocean. *Journal of Geophysical Research Oceans, 122*(3), 2012–2028.

Meissner, T. & Wentz, F. J. (2018). Remote sensing sytems SMAP ocean surface salinities, Version 3.0 validated release. Remote Sensing Systems, Santa Rosa, CA, USA.

Meyers, M. P., Walko, R. L., Harrington, J. Y., & Cotton, W. R. (1997). New RAMS cloud microphysics parameterization. Part II: The two-moment scheme. *Atmospheric Research, 45*(1), 3–39.

Mikolajewicz, U., Sein, D. V., Jacob, D., Königk, T., Podzun, R., & Semmler, T. (2005). Simulating Arctic sea ice variability with a coupled regional atmosphere–ocean–sea ice model. *Meteorologische Zeitschrift, 14*(6), 793–800.

Neelin, J. D., Latif, M., Allaart, M. A. F., Cane, M. A., Cubasch, U., Gates, W. L., et al. (1992). Tropical air–sea interaction in general circulation models. *Climate Dynamics, 7*(2), 73–104.

Neu, U., Akperov, M. G., Bellenbaum, N., Benestad, R., Blender, R., Caballero, R., et al. (2013). IMILAST: A community effort to intercompare extratropical cyclone detection and tracking algorithms. *Bulletin of the American Meteorological Society, 94*(4), 529–547.

Nienhaus, M., Subrahmanyam, B., & Murty, V. S. N. (2012). Altimetric observations and model simulations of coastal Kelvin waves in the Bay of Bengal. *Marine Geodesy*. https://doi.org/10.1080/01490419.2012.718607.

Qiu, Y., Han, W., Lin, X., West, B. J., Li, Y., Xing, W., et al. (2019). Upper-ocean response to the super tropical cyclone Phailin (2013) over the freshwater region of the Bay of Bengal. *Journal of Physical Oceanography, 49*(5), 1201–1228.

Rao, R. R., Kumar, G. M. S., Ravichandran, M., Rao, A. R., Gopalakraishna, V. V., & Thadathil, P. (2010). Interannual variability of Kelvin wave propagation in the wave guides of the equatorial Indian Ocean, the coastal Bay of Bengal and the southeastern Arabian Sea during 1993–2006. *Deep Sea Research Part I Oceanographic Research papers, 57*(1), 1–13.

Ratnam, J. V., Giorgi, F., Kaginalkar, A., & Cozzini, S. (2009). Simulation of the Indian monsoon using the RegCM3–ROMS regional coupled model. *Climate Dynamics, 33*(1), 119–139.

Reale, M., Giorgi, F., Solidoro, C., Di Biagio, V., Di Sante, F., Mariotti, L., et al. (2020). The Regional Earth System Model RegCM-ES: Evaluation of the Mediterranean climate and marine biogeochemistry. *Journal of Advances in Modeling Earth Systems, 12*, e2019MS001812. https://doi.org/10.1029/2019MS001812.

Reale, M., Liberato, M. L., Lionello, P., Pinto, J. G., Salon, S., & Ulbrich, S. (2019). A global climatology of explosive cyclones using a multi-tracking approach. *Tellus A Dynamic Meteorology and Oceanography, 71*(1), 1611340.

Rinke, A., Gerdes, R., Dethloff, K., Kandlbinder, T., Karcher, M., Kauker, F., et al. (2003). A case study of the anomalous Arctic sea ice conditions during 1990: Insights from coupled and uncoupled regional climate model simulations. *Journal of Geophysical Research Atmospheres, 108*, D9. https://doi.org/10.1029/2002JD003146.

Rohith, B., Paul, A., Durand, F., et al. (2019). Basin-wide sea level coherency in the tropical Indian Ocean driven by Madden–Julian Oscillation. *Nature Communications*, *10*, 1257. https://doi.org/10.1038/s41467-019-09243-5.

Saleeby, S. M., & Cotton, W. R. (2004). A large-droplet mode and prognostic number concentration of cloud droplets in the Colorado State University Regional Atmospheric Modeling System (RAMS). Part I: Module descriptions and super cell test simulations. *Journal of Applied Meteorology, 43*(1), 182–195.

Saleeby, S. M., & Van den Heever, S. C. (2013). Developments in the CSU-RAMS aerosol model: Emissions, nucleation,

regeneration, deposition, and radiation. *Journal of Applied Meteorology and Climatology, 52*(12), 2601–2622.

Samala, B. K., Banerjee, S., Kaginalkar, A., & Dalvi, M. (2013). Study of the Indian summer monsoon using WRF–ROMS regional coupled model simulations. *Atmospheric Science Letters, 14*(1), 20–27.

Schade, L. R., & Emanuel, K. A. (1999). The ocean's effect on the intensity of tropical cyclones: Results from a simple coupled atmosphere-ocean model. *Journal of the Atmospheric Sciences*, *56*, 642–651.

Schrum, C. (2017). Regional climate modeling and air–sea coupling. *Oxford Research Encyclopedia of Climate Science*. https://doi.org/10.1093/acrefore/9780190228620.013.3.

Sein, D. V., Gröger, M., Cabos, W., Alvarez-Garcia, et al. (2020). Regionally coupled atmosphere–ocean–marine biogeochemistry model ROM: 2. Studying the climate change signal in the North Atlantic and Europe. *Journal of Advances in Modeling Earth Systems, 12*, 1. https://doi.org/10.1029/2019MS001646.

Sein, D. V., Mikolajewicz, U., Gröger, M., Fast, I., Cabos, W., Pinto, J. G., et al. (2015). Regionally coupled atmosphere-ocean-sea ice-marine biogeochemistry model ROM: 1. Description and validation. *Journal of Advances in Modeling Earth Systems, 7*(1), 268–304.

Seo, H., Murtugudde, R., Jochum, M., & Miller, A. J. (2008). Modeling of mesoscale coupled ocean–atmosphere interaction and its feedback to ocean in the western Arabian Sea. *Ocean Modelling, 25*(3–4), 120–131.

Shchepetkin, A., & McWilliams, J. (2005). *The regional ocean modeling system: A split-explicit, free-surface, topography-following-coordinate oceanic model*. Los Angeles: Institute of Geophysics and Planetary Physics, University of California.

Sitz, L. E., et al. (2017). Description and evaluation of the Earth System Regional Climate Model (Reg CM-ES). *Journal of Advances in Modeling Earth Systems*, *9*, 1863–1886.

Smith, W. H., & Sandwell, D. T. (1997). Global sea floor topography from satellite altimetry and ship depth soundings. *Science, 277*(5334), 1956–1962.

Somot, S., Sevault, F., Déqué, M., & Crépon, M. (2008). 21st century climate change scenario for the Mediterranean using a coupled atmosphere–ocean regional climate model. *Global and Planetary Change, 63*(2–3), 112–126.

Sreenivas, P., & Gnanaseelan, C. (2014). Impact of oceanic processes on the life cycle of severe cyclonic storm "Jal". *IEEE Geoscience and Remote Sensing Letters, 11*(2), 519–523.

Sreenivas, P., Gnanaseelan, C., & Prasad, K. V. S. R. (2012). Influence of El Niño and Indian Ocean Dipole on sea level variability in the Bay of Bengal. *Global and Planetary Change, 80*, 215–225.

Srinivas, C. V., Mohan, G. M., Naidu, C. V., Baskaran, R., & Venkatraman, B. (2016). Impact of air-sea coupling on the simulation of tropical cyclones in the North Indian Ocean using a simple 3-D ocean model coupled to ARW. *Journal of Geophysical Research Atmospheres, 121*(16), 9400–9421.

Sun, R., Subramanian, A. C., Miller, A. J., Mazloff, M. R., Hoteit, I., & Cornuelle, B. D. (2019). SKRIPS v1.0: A regional coupled ocean-atmosphere modeling framework (MITgcm-WRF) using ESMF/NUOPC, description and preliminary results for the Red Sea. *Geoscientific Model Development Discussions*. https://doi.org/10.5194/gmd-2018-252.

Sun, Y., Perrie, W., & Toulany, B. (2018). Simulation of wave–current interactions under hurricane conditions using an unstructured-grid model: Impacts on ocean waves. *Journal of Geophysical Research Oceans, 123*(5), 3739–3760.

Thorncroft, C., & Hodges, K. (2001). African easterly wave variability and its relationship to Atlantic tropical cyclone activity. *Journal of Climate*, *14*, 1166–1179.

Tuleya, R. E., & Kurihara, Y. (1981). A numerical study on the effects of environmental flow on tropical storm genesis. *Monthly Weather Review, 109*(12), 2487–2506.

Veeranjaneyulu, Ch., & Deo, A. A. (2019). Study of upper ocean parameters during passage of tropical cyclones over Indian seas. *International Journal of Remote Sensing, 40*(12), 4683–4723.

Walko, R. L., Band, L. E., Baron, J., Kittel, T. G., Lammers, R., Lee, T. J., et al. (2000). Coupled atmosphere–biophysics–hydrology models for environmental modeling. *Journal of Applied Meteorology, 39*(6), 931–944.

Walko, R. L., Cotton, W. R., Meyers, M. P., & Harrington, J. Y. (1995). New RAMS cloud microphysics parameterization part I: The single-moment scheme. *Atmospheric Research, 38*(1–4), 29–62.

Warner, J. C., Armstrong, B., He, R., & Zambon, J. B. (2010). Development of a coupled ocean–atmosphere–wave–sediment transport (COAWST) modeling system. *Ocean Model*, *35*, 230–244.

Yan, Y., Li, L., & Wang, C. (2017). The effects of oceanic barrier layer on the upper ocean response to tropical cyclones. *Journal of Geophysical Research Oceans, 122*(6), 4829–4844.

Zhang, Z., Zhang, Y., & Wang, W. (2017). Three-compartment structure of subsurface-intensified mesoscale eddies in the ocean. *Journal of Geophysical Research Oceans, 122*(3), 1653–1664.

Zou, L., & Zhou, T. (2013). Can a regional ocean–atmosphere coupled model improve the simulation of the interannual variability of the western North Pacific summer monsoon? *Journal of Climate, 26*(7), 2353–2367.